

First-principles wavevector- and frequency-dependent exchange-correlation kernel for jellium and related metals

Aaron D. Kaplan,^{1,*} Niraj K. Nepal,¹ Adrienn Ruzsinszky,¹ Pietro Ballone,² and John P. Perdew^{1,3,†}

¹*Department of Physics, Temple University, Philadelphia, PA 19122, USA*

²*School of Physics and Conway Institute for Biomolecular and Biomedical Research, University College, Dublin, Ireland*

³*Department of Chemistry, Temple University, Philadelphia, PA 19122, USA*

(Dated: June 25, 2022)

We propose a spatially and temporally nonlocal exchange-correlation (xc) kernel for the spin-unpolarized fluid phase of ground-state jellium, for use in time-dependent density functional and linear response calculations. The kernel is constructed to satisfy known properties of the exact xc kernel, to accurately describe the correlation energies of bulk jellium, and to satisfy frequency-moment sum rules at a wide range of bulk jellium densities. All exact constraints satisfied by the recent MCP07 kernel [A. Ruzsinszky, *et al.*, Phys. Rev. B 101, 245135 (2020)] are maintained in the new tightly-constrained 2021 (TC21) kernel, while others are added.

I. INTRODUCTION

Ground-state density functional theory (g.s. DFT) [1] is a mature field that yields exact-in-principle ground-state energies and densities of any non-relativistic many-electron system. Practical applications of g.s. DFT require approximations to the “exchange-correlation” energy E_{xc} , the simplest of which, the local density approximation (LDA) predates modern g.s. DFT. Modern approximations to the xc energy can make reasonable predictions of g.s. properties, often comparable to experiment.

Ground state DFT can be extended to the time domain to include either arbitrary [2] or weak [3, 4] time-dependent external potentials (TD-DFT). Within the exact theory or the linear-response regime, the xc potential rather than the xc energy must be approximated. The xc kernel f_{xc} is related to the exchange correlation potential v_{xc} via functional differentiation

$$f_{xc}(\mathbf{r}, t; \mathbf{r}', t') = \frac{\delta v_{xc}(\mathbf{r}, t)}{\delta n(\mathbf{r}', t')} \theta(t - t') \quad (1)$$

with $\theta(y > 0) = 1$, and $\theta(y < 0) = 0$. f_{xc} can be computed from the second functional derivative of E_{xc} from a g.s. calculation only in an adiabatic approximation (assuming the response is local in time). Approximate expressions for E_{xc} used in g.s. calculations do not necessarily provide similarly accurate adiabatic approximations to f_{xc} for use in TD-DFT calculations.

Thus, highly-accurate approximations to the exact f_{xc} are needed for realistic descriptions of materials. G.S. DFT is instructive in this regard: functionals that are most broadly transferrable, e.g., that of Ref. [5], are designed to satisfy known limiting behaviors of the exact E_{xc} . These include the uniform density (jellium) limit, gradient expansions for slowly-varying metallic densities, and scaling relations.

Recently, an approximate, dynamic kernel for jellium was proposed with similar construction principles. Jellium is characterized by a uniform electron density $n = 3/(4\pi r_s^3) = k_F^3/(3\pi^2)$. In this work, we will use Hartree atomic units, $\hbar = m_e = e^2 = 1$, for all quantities and numerical coefficients, unless noted otherwise. The modified Constantin-Pitarke 2007 (MCP07) [6] kernel is constructed as an interpolation between static $f_{xc}(q, \omega = 0)$ and long-wavelength dynamic $f_{xc}(q = 0, \omega)$ limits,

$$f_{xc}^{MCP07}(q, \omega) = \left\{ 1 + e^{-kq^2} \left[\frac{f_{xc}(0, \omega)}{f_{xc}(0, 0)} - 1 \right] \right\} f_{xc}^{MCP07}(q, 0). \quad (2)$$

In this equation, $f_{xc}(0, \omega)$ is the Gross-Kohn-Iwamoto (GKI) kernel [3, 7], which satisfies known analytic and asymptotic $\omega \rightarrow \infty$ behaviors of the exact $f_{xc}(0, \omega)$. The static limit is controlled by $f_{xc}^{MCP07}(q, 0)$, a revision to the Constantin-Pitarke static kernel [8] that enforces known exact constraints on the short-wavelength limit $f_{xc}(q \rightarrow \infty, 0)$, as well as the gradient expansion of $f_{xc}(q, 0)$ for slowly-varying densities. $f_{xc}(0, 0)$ is the adiabatic local density approximation (ALDA), found as the $q \rightarrow 0$ limit of the Fourier transform of $\frac{\delta^2 E_{xc}}{\delta n(\mathbf{r}) \delta n(\mathbf{r}'')}$ evaluated at the uniform density n . The order in which the $|\mathbf{q}| \rightarrow 0$ and $\omega \rightarrow 0$ limits are taken yields different limiting behaviors for the exact f_{xc} , as discussed in Appendix C. For MCP07 and our model f_{xc} , we make the simplifying approximation that either order of limits yields the ALDA f_{xc} . The inverse-squared screening wavevector

$$k = -\frac{f_{xc}(0, 0)}{4\pi B(r_s)} \quad (3)$$

with $B(r_s)$ parameterized by Eq. 7 of Ref. [9], was chosen to enforce two separate exact constraints on the static kernel $f_{xc}(q, \omega = 0)$ [6]

$$\lim_{q \rightarrow 0} \left[\lim_{\omega \rightarrow 0} f_{xc}(q, \omega) \right] = f_{xc}(0, 0) \quad (4)$$

$$\lim_{q \rightarrow \infty} \left[\lim_{\omega \rightarrow 0} f_{xc}(q, \omega) \right] = -4\pi \left[\frac{C(r_s)}{k_F^2} + \frac{B(r_s)}{q^2} \right]. \quad (5)$$

* kaplan [at] temple.edu

† perdew [at] temple.edu

$C(r_s)$ is given by Eq. A2 of Ref. [8]. However, k also appears in the dynamic MCP07 to control the interpolation in Eq. 2 between the non-uniform static and uniform dynamic limits. This choice was made consistent with Occam’s razor: Other things being equal, the simplest hypothesis is to be preferred. We will investigate the effect of modifying this length scale.

It should be kept in mind that the random phase approximation (RPA), which sets $f_{xc}^{\text{RPA}} = 0$, includes exchange effects and long-range correlation effects exactly in metals [10]. The RPA lacks an accurate description of short-range correlation [11], which is typically better described by semi-local *g.s.* energy *functionals* (depending only upon the electron density and its spatial derivatives), motivating the family of RPA+ energy functionals [12]. These can provide highly-accurate descriptions of metals, but do not test f_{xc} . In RPA+, a local or semi-local correction is added to RPA.

Although the ALDA, by definition, provides a better description of short-range correlation than does the RPA, ALDA does not generally make better predictions than RPA. This can be seen clearly in Fig. S10 of Ref. [13] which plots jellium correlation energies per electron ε_c : the RPA makes ε_c too negative, whereas the ALDA overcorrects RPA at all densities. The ALDA also predicts onset of a static charge density wave for $r_s \approx 30$, not in line with quantum Monte Carlo (QMC) predictions for Wigner crystallization at $r_s \approx 85 \pm 20$ [14].

Extensive tests of the MCP07 functional for real systems are not currently available, and not without good reason, as we shall discuss shortly. However, it was observed in Ref. [13] that the MCP07 kernel can be improved in two regards: a more accurate recovery of jellium correlation energies at all densities, and better satisfaction of the third frequency-moment sum rule (see, for example, Eq. 3.142 of Ref. [15]) for low-density jellium. This motivates the main inquiry of this paper: by improving the MCP07 kernel for paradigmatic metallic systems (jellium at all densities) and for known exact sum rules, can we make an xc kernel based on a jellium paradigm that provides physically realistic descriptions of many solid-state systems?

To better emphasize the construction principles underlying the new XC kernel, we refer to this new kernel as the Tightly Constrained 2021 (TC21) kernel.

We will demonstrate the versatility of this kernel by calculating physical quantities that have interpretations in real systems, and not with self-consistent calculations. A few freely available codes, e.g., GPAW [16] and the DP code [17], can perform self-consistent TD-DFT calculations in solids using a model $f_{xc}(q, \omega)$ as input. However, obtaining well-converged solutions in real systems is often extremely challenging, and deserves due attention in a dedicated computational work. As this is beyond the scope of the current work, we will instead focus on direct applications of the TC21 kernel to physical properties, such as screening due to a weak perturbation. As another direct application of our kernel, one could use Eqs.

21 and 23 of Ref. [18] to construct a fully nonlocal approximation to the exchange-correlation potential for a given density.

There are practical limitations to using a model $f_{xc}[n](q, \omega)$ in TD-DFT codes. If, for all real frequencies, only the imaginary part of the kernel is defined in closed form, the real part must be computed by a Kramers-Kronig relation. If the kernel is defined in closed form only at real frequency, one must then analytically continue the kernel to imaginary frequencies to efficiently compute correlation energies, as will be discussed. The continuation is typically done by numeric integration, or Taylor expansion. The cost of repeated numeric integration (or series expansion) compounds substantially. Our solutions to these problems will be discussed in Section 2.

II. REVISED MCP07 XC KERNEL: TC21

We begin by re-parameterizing $\text{Re } f_{xc}(0, \omega)$ at real frequencies ω . Note that the Gross-Kohn-Iwamoto kernel proposes only an imaginary part of $f_{xc}(q = 0, \omega)$, and the real part must be constructed via the Kramers-Kronig relation

$$\text{Re } f_{xc}(0, \omega) - f_{xc}(0, \infty) = \frac{1}{\pi} \text{P} \int_{-\infty}^{\infty} \frac{\text{Im } f_{xc}(0, u)}{u - \omega} du. \quad (6)$$

Iwamoto and Gross determined the infinite-frequency limit to be [7]

$$f_{xc}(0, \infty) = -\frac{1}{5} \frac{3\pi}{k_F^2} - \frac{1}{15n} \left[22\varepsilon_c^{\text{UEG}} + 26r_s \frac{d\varepsilon_c^{\text{UEG}}}{dr_s} \right], \quad (7)$$

with $\varepsilon_c^{\text{UEG}}$ the correlation energy per electron in a uniform electron gas (UEG). Ref. [13] determined that the frequency-dependence of the MCP07 kernel at “intermediate” r_s (particularly $r_s = 69$) was likely in error, as the static structure factor, or spectral function,

$$S(\mathbf{q}) = \int_0^{\infty} S(\mathbf{q}, \omega) d\omega \quad (8)$$

exhibited unphysically large peaks [19], as compared to previously unpublished QMC data shown in Fig. 12 of Appendix B. Here, we define the term “intermediate” densities as that range of densities between normal metallic densities ($1 \lesssim r_s \lesssim 10$) and the Wigner crystal phase of jellium ($r_s \gtrsim 85$). Thus we will use “intermediate density” to refer to the approximate range $10 \lesssim r_s \lesssim 100$. The dynamic structure factor

$$S(\mathbf{q}, \omega) = -\frac{1}{\pi n} \text{Im } \chi(\mathbf{q}, \omega) \quad (9)$$

is determined by the adiabatic-connection fluctuation-dissipation theorem [20, 21] for the interacting density-density response function

$$\chi(\mathbf{q}, \omega) = \frac{\chi_0(\mathbf{q}, \omega)}{1 - [4\pi/q^2 + f_{xc}(\mathbf{q}, \omega)]\chi_0(\mathbf{q}, \omega)}, \quad (10)$$

and $\chi_0(\mathbf{q}, \omega)$ is the non-interacting, or Kohn-Sham, response function [22].

In the MCP07 kernel, $\text{Re } f_{xc}(0, \omega)$ is parametrized as

$$\text{Re } f_{xc}(0, \omega) = f_{xc}(0, \infty) - cb^{3/4}(n)h(b^{1/2}(n)\omega), \quad (11)$$

$$b(n) = \left\{ \frac{\gamma}{c} [f_{xc}(0, \infty) - f_{xc}(0, 0)] \right\}^{4/3} \quad (12)$$

where $\gamma = \Gamma(\frac{1}{4})^2 / (32\pi)^{1/2}$, and $c = 23\pi/15$ are determined from the static and infinite frequency limits of $\text{Im } f_{xc}(0, \omega)$ [3]. The dimensionless function $h(X)$ enforces these limits

$$\lim_{X \rightarrow 0} h(X) \rightarrow \frac{1}{\gamma} \quad (13)$$

$$\lim_{\omega \rightarrow \infty} \text{Re } f_{xc}(0, \omega) \rightarrow f_{xc}(0, \infty) + \frac{c}{\omega^{3/2}} \quad (14)$$

while modeling the finite frequency dependence of $\text{Re } f_{xc}(0, \omega)$ through the Kramers-Kronig principal value integral. As noted in the Introduction, repeated evaluation of $\text{Re } f_{xc}(0, \omega)$ through the Kramers-Kronig integral is computationally expensive. Therefore, an accurate model of the Kramers-Kronig-derived frequency dependence through h is an essential component of an analytic and numerically efficient $f_{xc}(0, \omega)$. Figure 4 of Ref. [6] shows that h adequately models this frequency dependence, however h can be improved. We propose a simple modification to the MCP07 $h(X)$ function

$$h(X) = \frac{1}{\gamma} \frac{1 - c_1 X^2}{[1 + c_2 X^2 + c_3 X^4 + c_4 X^6 + (c_1/\gamma)^{16/7} X^8]^{7/16}}, \quad (15)$$

where the parameters

$$c_1 = 0.17467008438086054 \quad (16)$$

$$c_2 = 3.2237984506125503 \quad (17)$$

$$c_3 = 2.224790597667039 \quad (18)$$

$$c_4 = 1.8906775733050594 \quad (19)$$

were determined by directly fitting to numeric Kramers-Kronig results. Note that h is an even function of real-valued frequency. (Note that an exact expression is given in Eq. 4.84 of Ref. [23], however this expression involves nonstandard special functions.)

We also need to analytically continue the GKI kernel to imaginary frequencies. As this case is useful for the evaluation of the correlation energy, the analytic continuation to purely imaginary frequencies can be accurately represented by

$$f_{xc}(0, iu) \approx -cb^{3/4}(n)j(b^{1/2}(n)u) + f(0, \infty) \quad (20)$$

$$j(y) = \frac{1}{\gamma} \frac{1 - k_1 y + k_2 y^2}{[1 + k_3 y^2 + k_4 y^4 + k_5 y^6 + (k_2/\gamma)^{16/7} y^8]^{7/16}} \quad (21)$$

$$k_1 = 1.2246033094646769 \quad (22)$$

$$k_2 = 0.9780663544436814 \quad (23)$$

$$k_3 = 0.395541393738581 \quad (24)$$

$$k_4 = 1.3302298569459192 \quad (25)$$

$$k_5 = 1.0056767945146443 \quad (26)$$

with the k_i determined by a non-linear least-squares fit to an r_s -independent form, and $u \geq 0$ is purely real.

In this work, we will use the Perdew-Wang parametrization [24] of the correlation energy per electron in jellium, as this yields an improved, smoother fit to quantum Monte-Carlo data [14] than does the Perdew-Zunger parametrization [25] used for $f_{xc}(0, 0)$ in the MCP07 kernel. Reference [13] also made it clear that the r_s -dependence of the MCP07 kernel does not adequately reproduce the correlation energies per electron in jellium. The correlation energy per particle is given by the multi-dimensional integral [10]

$$\varepsilon_c = \frac{1}{2} \int \frac{d^3 q}{(2\pi)^3} \int_0^1 \frac{d\lambda}{\lambda} \int_0^\infty d\omega \frac{4\pi\lambda}{q^2} [S_\lambda(\mathbf{q}, \omega) - S_0(\mathbf{q}, \omega)], \quad (27)$$

where $f_{xc,\lambda}(\mathbf{q}, \omega, r_s) = \lambda^{-1} f_{xc}(\lambda^{-1}\mathbf{q}, \lambda^{-2}\omega, \lambda r_s)$ [26] and S_λ is evaluated using the coupling-constant λ -scaled f_{xc} . Note that $S_0(\mathbf{q}, \omega) = -\text{Im } \chi_0(\mathbf{q}, \omega) / (\pi n)$. We adopt a similar integration scheme as Ref. [13] to evaluate correlation energies per particle, but use a grid with a fixed number of points chosen to recover the RPA values reported there.

The ‘‘screening’’ wavevector k in Eq. 2 for the dynamic MCP07 kernel was chosen to be identical to the wavevector appearing in the static part of the MCP07 kernel. That choice was made consistent with an Occam’s Razor-style construction principle: free parameters should be avoided when possible.

Consider the revision

$$f_{xc}(q, \omega) = \left\{ 1 + e^{-(q/\tilde{k})^2} \left[\frac{f_{xc}(0, \Omega)}{f_{xc}(0, 0)} - 1 \right] \right\} f_{xc}^{\text{MCP07}}(q, 0) \quad (28)$$

$$\Omega = p(r_s, q)\omega \quad (29)$$

$$\tilde{k} = \frac{Ak_F}{1 + Bk_F^{1/2}}, \quad (30)$$

$$p(r_s, q) = Cr_s^2 + (1 - Cr_s^2) \exp[-D(q/\tilde{k})^2] \quad (31)$$

where

$$A = 4.470217788196006 \quad (32)$$

$$B = 1.4327137309889693 \quad (33)$$

$$C = 0.04466295040605292 \quad (34)$$

$$D = 2.918135781120395 \quad (35)$$

were determined by minimizing the normalized, unweighted sum

$$\sigma = \left(\sum_{r_s} 1 \right)^{-1} \sum_{r_s} |\varepsilon_c^{\text{TC21}}(r_s) - \varepsilon_c^{\text{PW92}}(r_s)|. \quad (36)$$

For the fit, the set $r_s \in \{1, 2, 3, \dots, 98, 99, 100\}$ was used to determine A , B , C , and D . Over-fitting is avoided by using a large number of r_s values and a fixed integration grid, where numeric convergence is not guaranteed

to identical precision for each r_s . Figure S10 of Ref. [13] shows that $\varepsilon_c^{\text{MCP07}}$ is least accurate at intermediate r_s , motivating the factor of r_s^2 in Eq. 31. The accuracy of the TC21 kernel at intermediate densities is greatly improved, as seen in Fig. 1. The TC21 kernel also represents an accurate extrapolation to $r_s > 100$ and $r_s < 1$.

At low densities, exchange and correlation have the same length scale, the Fermi wavelength $2\pi/k_F$. Accordingly, at low densities, $\tilde{k} \propto k_F$. At high densities, the appropriate length scale for correlation is the inverse of the Thomas-Fermi wavevector, $k_{\text{TF}} = \sqrt{4k_F/\pi}$. Thus, $\tilde{k} \propto k_{\text{TF}}$ at high densities.

There is existing precedence for scaling the frequency-dependent part of the kernel by a function of q , as we have by introducing $\Omega(r_s, q, \omega)$. Dabrowski [27] sought to extend the long-wavelength Gross-Kohn kernel [3] to nonzero q by enforcing zero and infinite [28] frequency limits on the spin-symmetric local field factor [15]

$$G_+(q, \omega) = \frac{1}{2}[G_{\uparrow\uparrow}(q, \omega) + G_{\uparrow\downarrow}(q, \omega)] = -\frac{q^2}{4\pi}f_{\text{xc}}(q, \omega). \quad (37)$$

The Dabrowski kernel is limited in that it uses older expressions for the static local field factors [29–31] which have no closed form, and predated the work of Iwamoto and Gross [7], which corrected the Gross-Kohn expression to enforce the third frequency-moment sum rule.

It should also be noted that the spin-antisymmetric local field factor $G_-(q, \omega) = [G_{\uparrow\uparrow}(q, \omega) - G_{\uparrow\downarrow}(q, \omega)]/2$ is needed to describe the spin-spin response function

$$\chi_{ss'}(\mathbf{q}, \omega) = \frac{\chi_0(\mathbf{q}, \omega)}{1 - 4\pi/q^2[1 - G_-(q, \omega)]\chi_0(\mathbf{q}, \omega)}, \quad (38)$$

At present, we lack sufficient information to determine a first-principles, spin-polarized f_{xc} from the uniform electron gas. Works like those of Richardson and Ashcroft [32] are therefore useful in understanding the spin-spin response, which is needed to describe two-electron interactions [33], such as those that spur formation of Cooper pairs. It is important to note that spin resolution is still implicitly included in $f_{\text{xc}}(q, \omega)$, even if it is not decomposed into same- and opposite-spin components. This is in stark contrast to some approximate expressions for G_+ which assume $G_{\uparrow\downarrow} \approx 0$, thereby neglecting all correlation interactions. A spin decomposition of the ALDA is given in Ref. [34].

Our kernel retains the broad features of these earlier works. It may well be possible to enforce known limits on $G(q, \omega)$, however all existing work is r_s -dependent, primarily in a metallic range $1 \lesssim r_s \lesssim 10$. Real solids have regions of significant density depletion (e.g., vacancies and voids in semiconductors). By constraining the model kernel to recover accurate jellium energetics at a wide range of densities, we hope to better describe real systems.

A similar approach was taken by Panholzer *et al.* [35], who directly tabulated highly accurate expressions for $f_{\text{xc}}(q, \omega)$ in jellium at a range of densities $0.8 \leq r_s \leq$

r_s	ε_c PW92	RPA	ALDA	MCP07	TC21
0.1	-0.1209	-0.1441	-0.1084	-0.1286	-0.1267
0.2	-0.1011	-0.1235	-0.0886	-0.1079	-0.1061
0.3	-0.0900	-0.1118	-0.0775	-0.0961	-0.0945
0.4	-0.0824	-0.1036	-0.0698	-0.0880	-0.0864
0.5	-0.0766	-0.0974	-0.0640	-0.0818	-0.0803
0.6	-0.0720	-0.0924	-0.0593	-0.0769	-0.0754
0.7	-0.0682	-0.0882	-0.0555	-0.0728	-0.0713
0.8	-0.0650	-0.0847	-0.0522	-0.0692	-0.0678
0.9	-0.0622	-0.0816	-0.0494	-0.0662	-0.0648
1	-0.0598	-0.0788	-0.0469	-0.0635	-0.0622
2	-0.0448	-0.0618	-0.0316	-0.0469	-0.0459
3	-0.0369	-0.0528	-0.0236	-0.0382	-0.0375
4	-0.0319	-0.0469	-0.0183	-0.0325	-0.0321
5	-0.0282	-0.0424	-0.0143	-0.0283	-0.0282
6	-0.0254	-0.0390	-0.0111	-0.0250	-0.0251
7	-0.0232	-0.0364	-0.0087	-0.0226	-0.0230
8	-0.0214	-0.0342	-0.0066	-0.0205	-0.0212
9	-0.0199	-0.0322	-0.0048	-0.0187	-0.0196
10	-0.0186	-0.0306	-0.0032	-0.0173	-0.0183

TABLE I. Jellium correlation energies per particle, in hartree/electron, for a variety of XC kernels and PW92. For a plot of ε_c on the range $0.1 \leq r_s \leq 120$, see Fig. 1. The values of ε_c were determined using the same integration grid used to fit the TC21 parameters.

8, frequencies and wavevectors, as well as a prescription for interpolating it (a “connector”). Many-body theory approaches can also be used to tabulate the dielectric function of jellium, as was done in Ref. [36] for the static response. Our approach may yield greater generality.

These modifications also soften the peak structure seen in $S(q)$ for $r_s = 69$. Figures 2 and 3 show clearly that the large MCP07 peak in the $r_s = 69$ curve is reduced substantially, while the $r_s = 4$ curve is essentially unchanged. It is difficult to determine what $S(q)$ should look like at all densities. A parameterization of the jellium $S(q)$ from QMC data for $r_s \leq 10$ [37] suggests a monotonic increasing $S(q)$ at most densities. At intermediate densities, this parameterization represents an extrapolation of unknown accuracy; previously unpublished QMC data [19] at lower densities suggests that $S(q)$ is nonmonotonic, as shown in Fig. 12 of Appendix B.

III. CHARACTERIZING THE TC21 KERNEL

A. Static charge density wave in jellium

Here we will discuss the appearance of a static charge-density wave in jellium at low density. A first-order phase transition often occurs close to a singularity in a linear response function, in our case $\chi(\mathbf{q}, \omega)$ of Eq. 10. Let $k_{\text{F},c}$ be

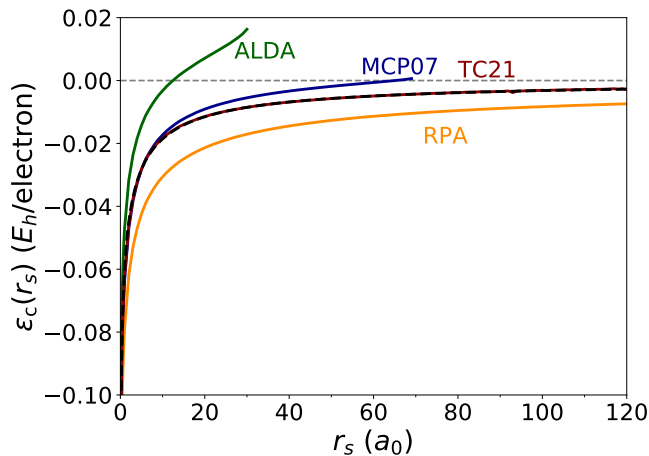


FIG. 1. Demonstrating the higher accuracy of the TC21 kernel in predicting jellium correlation energies per electron (in units of hartrees E_h per electron; note that $1E_h \approx 27.211$ eV) at a range of densities (in units of bohr radii $a_0 \approx 0.529\text{\AA}$). PW92 [24] (black, dashed) is essentially exact. For the values plotted here in the range $0.1 \leq r_s \leq 10$, see Table I.

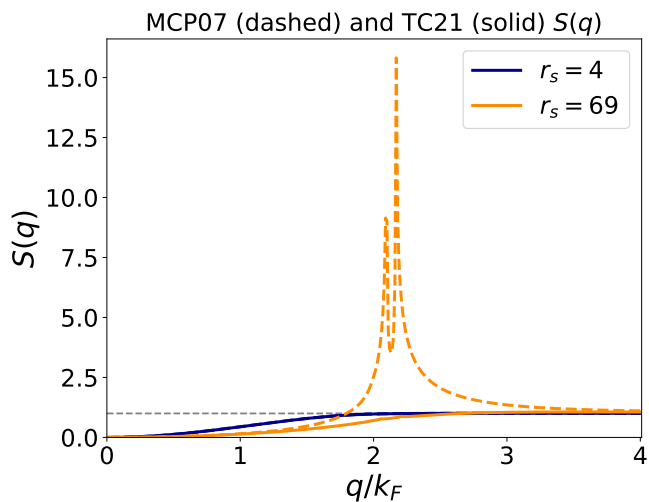


FIG. 2. Comparison of the static structure factors $S(q)$ for the MCP07 (dashed) and TC21 (solid) kernels at a higher, $r_s = 4$ (blue), and much lower, $r_s = 69$ (orange), density. The TC21 kernel almost completely eliminates the unphysically large peak structure seen in the MCP07 kernel at lower densities. For the TC21 spectral function alone, see Fig. 3.

the critical Fermi wavevector [and $r_{s,c} = (9\pi/4)^{1/3}/k_{F,c}$] such that the static dielectric function

$$\tilde{\epsilon}[n](q, 0) = 1 - \left[\frac{4\pi}{q^2} + f_{xc}[n](q, 0) \right] \chi_0[n](q, 0) \quad (39)$$

vanishes. The results of this calculation, comparable to Fig. 2 of Ref. [6], are shown in Fig. 4. As reported there, we find that $r_{s,c} \approx 30$ for the ALDA, and $r_{s,c} \approx 69$ for MCP07; for TC21, $r_{s,c} \approx 68$, exceedingly similar to MCP07. It should be noted that MCP07 and TC21 do

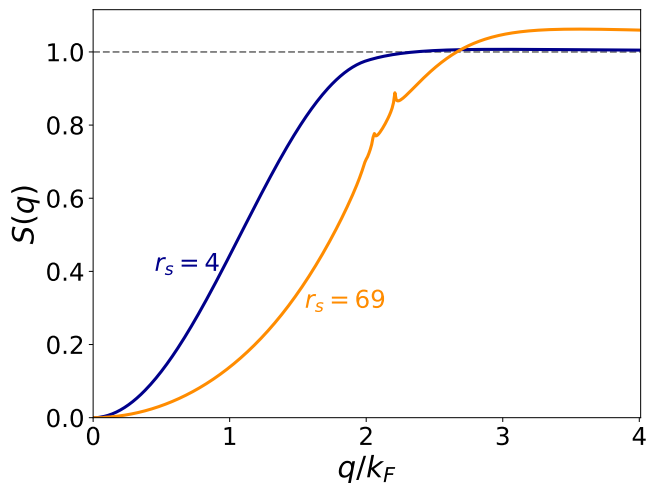


FIG. 3. The static structure factor $S(q)$ of the TC21 kernel.

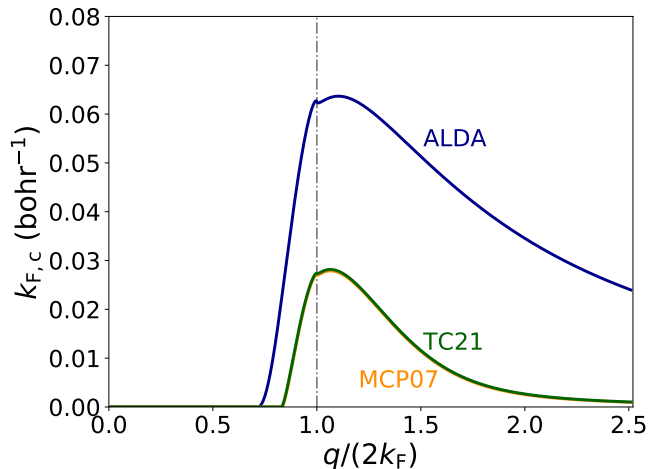


FIG. 4. Plot of the critical Fermi wavevector $k_{F,c}$, or equivalently, critical Wigner-Seitz radius $r_{s,c}$, such that the static dielectric function of Eq. 39 vanishes in jellium, signaling possible onset of a static charge density wave. For the RPA $k_{F,c} = 0$ at seemingly all wavevectors.

not have the same static limit, because of the different parameterizations of the ALDA used.

B. Sum rules

An important set of constraints on the spectral function are frequency-moment sum rules of the form

$$\Sigma_M(q) \equiv \int_0^\infty \omega^M S(q, \omega) d\omega, \quad (40)$$

where Σ_M is ostensibly known. For example, the “ f -sum” rule (see Eq. 3.141 of Ref. [15]) states that the

r_s	MURE MCP07	q_{MURE}/k_F	MURE TC21	q_{MURE}/k_F
4	0.048	2.06	0.044	2.05
10	0.125	2.16	0.092	2.31
30	0.358	2.29	0.166	2.64
69	0.808	2.42	0.210	3.00
100	0.830	2.86	0.183	3.00

TABLE II. Comparison of the maximum unsigned relative errors (MURE) for MCP07 and TC21 in the third moment sum rule calculation, and the corresponding value of q_{MURE}/k_F where the maximum occurs. As shown in Figs. 5 and 6, the relative error is defined as the difference between the left and right hand sides of Eq. 42, divided by their sum.

first frequency moment, in jellium

$$\Sigma_1(q) = \frac{q^2}{2}, \quad (41)$$

which was already well-satisfied by MCP07 [13]. Reference [13] demonstrated that MCP07 struggled with the third frequency-moment sum rule (see Eq. 3.142 of Ref. [15])

$$\Sigma_3(q) = \frac{q^2}{2} \left\{ \frac{q^4}{4} + 4\pi n + 2q^2(t_0 + t_c) + \frac{1}{\pi} \int_0^\infty dk \int_{-1}^1 du k^2 u^2 [S(\sqrt{q^2 + k^2 - 2kqu}) - S(k)] \right\} \quad (42)$$

in jellium at low densities. In Eq. 42, $t_0 = \frac{3}{10}k_F^2$ is the non-interacting kinetic energy per electron in jellium, and t_c is the interacting kinetic energy per electron. As t_c is not known exactly, we use the parameterization of Ref. [24],

$$t_c = -4\varepsilon_c(r_s, 0) + 3v_c(r_s, 0), \quad (43)$$

where $\varepsilon_c(r_s, \zeta)$ is the correlation energy per electron of jellium, $v_c = \partial(n\varepsilon_c)/\partial n$ is the corresponding (g.s.) correlation potential, and $\zeta = (n_\uparrow - n_\downarrow)/n$ is the relative spin-polarization, which we take to be zero.

The TC21 kernel satisfies the third moment sum rule nearly exactly at a range of densities, as shown in Fig. 5. This figure was generated in much the same way as Fig. S9 of Ref. [13], however the integration cutoff was set to $k_c = 14k_F$, much larger than the cutoff used there ($\sim 4k_F$). Moreover, a careful extrapolation to $k > k_c$ was made.

For comparison, Fig. 6 shows the relative error in the MCP07 third moment sum rule calculation using the higher cutoff. Note that for both the MCP07 kernel and the TC21 kernel, increasing the cutoff to $30k_F$ introduces large numeric instabilities in the integration. The maximum errors made by both kernels are tabulated in Table II.

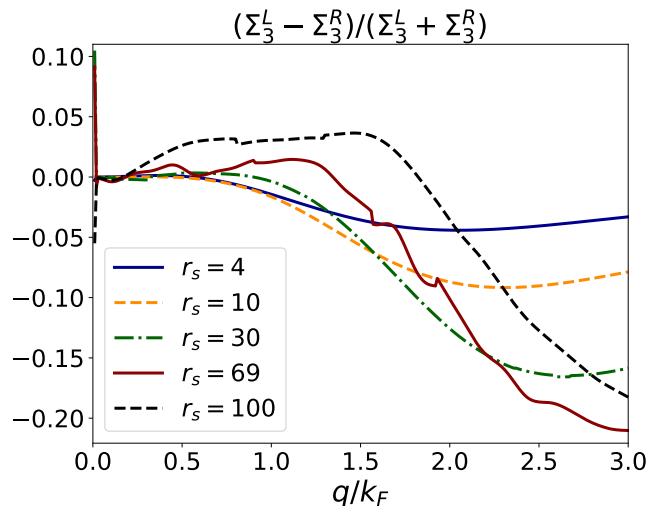


FIG. 5. Relative errors in the third-frequency moment sum rule of Eq. 42 for TC21. Σ_3^L represents the left-hand side of Eq. 42 $[\int_0^\infty \omega^3 S(q, \omega) d\omega]$, and Σ_3^R the right-hand side of Eq. 42. The third moment sum rule is satisfied nearly exactly by TC21 at a wide range of densities of jellium.

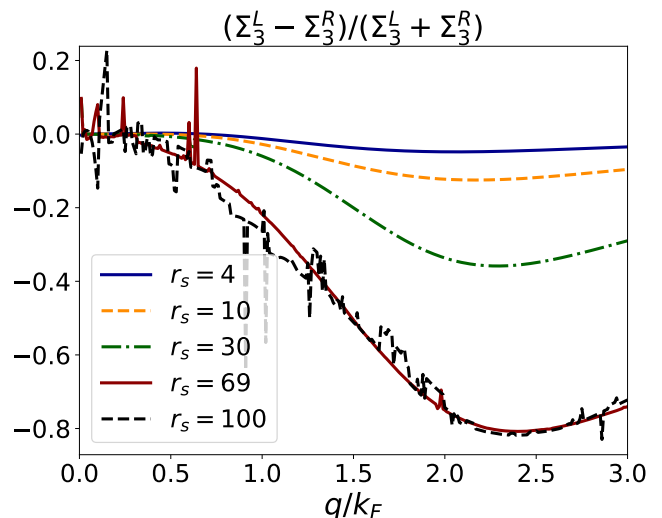


FIG. 6. Relative errors in the third-frequency moment sum rule of Eq. 42 for MCP07. Σ_3^L represents the left-hand side of Eq. 42 $[\int_0^\infty \omega^3 S(q, \omega) d\omega]$, and Σ_3^R the right-hand side of Eq. 42. The third moment sum rule is satisfied only approximately in MCP07 at intermediate to low density jellium. These results use a higher integration cutoff $k_c = 14k_F$ for $r_s \geq 10$ jellium.

C. Dressed interaction

Within density response theory, the dressed interaction (the effective electron-electron interaction that makes the random phase approximation exact)

$$v_{\text{eff}}(q, \omega) = v_{\text{bare}}(q) + f_{\text{xc}}(q, \omega), \quad (44)$$

where the bare interaction is $v_{\text{bare}}(q) = 4\pi/q^2$, is of central importance, as shown by Eq. 10. As q grows large, it is possible for v_{eff} to become negative; similarly, the dielectric function

$$\tilde{\epsilon}(q, \omega) = 1 - v_{\text{eff}}(q, \omega)\chi_0(q, \omega) \quad (45)$$

may become negative, as seen in Figs. 10 and 11 of the Appendix. The dressed interactions are plotted for the TC21 kernel at $r_s = 4$ and 69 in Figs. 7 and 8 respectively. At metallic densities and at intermediate densities, the effective potential becomes attractive only for $q \gtrsim k_F$.

The scaled frequency Ω entering TC21 is always greater or equal to the frequency ω . Thus at all densities, the TC21 kernel more rapidly approaches the infinite frequency limit than does MCP07. These differences are discernible in the dressed interaction at metallic densities. Moreover, as r_s increases, the differences become more pronounced, as Ω grows with r_s^2 for $q \gtrsim \tilde{k}$. For example, at $r_s = 69$, the TC21 dressed interaction has approached its infinite frequency limit for $\omega \approx \omega_p(0)$, whereas the MCP07 kernel tends closely to its static limit for $\omega = \omega_p(0)$.

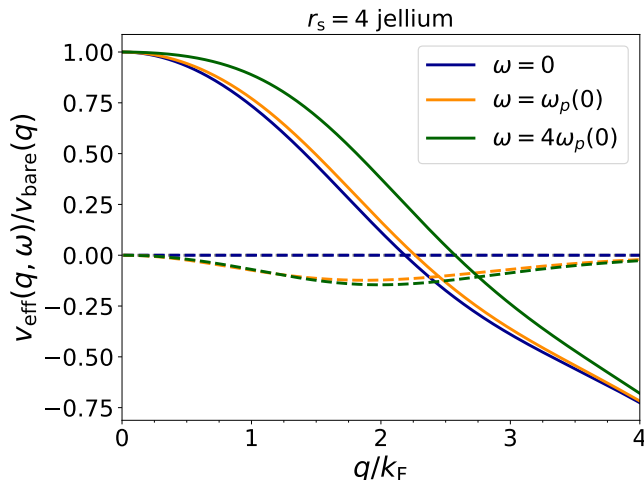


FIG. 7. Real (solid) and imaginary (dashed) parts of the scaled effective potential $v_{\text{eff}}/v_{\text{bare}}$ for $r_s = 4$ bulk jellium with the TC21 kernel. The crossings are $\text{Re } v_{\text{eff}}(2.185k_F, 0) = 0$, $\text{Re } v_{\text{eff}}(2.264k_F, \omega_p(0)) = 0$, and $\text{Re } v_{\text{eff}}(2.573k_F, 4\omega_p(0)) = 0$.

There are numerous interpretations of a negative dressed interaction or negative dielectric function [38], so we mention only a few here. These conditions imply that the screened interaction is attractive, which may underly unconventional mechanisms of superconductivity. The Kohn-Luttinger [39] theory posits that Friedel oscillations (characteristic of jellium and simple metal surfaces) lead to regions of attractive dressed interactions, allowing for Cooper pairing without consideration of electron-phonon interactions. A first-principles description of superconductivity using a $v_{\text{eff}}(q, \omega)$ derived

from a well-constrained local field factor [32] was developed by Richardson and Ashcroft [40]. For a phenomenological review of attractive quasiparticle interactions, see Ref. [41]; for the relationship between the dielectric function and high T_c superconductors, see Ref. [38].

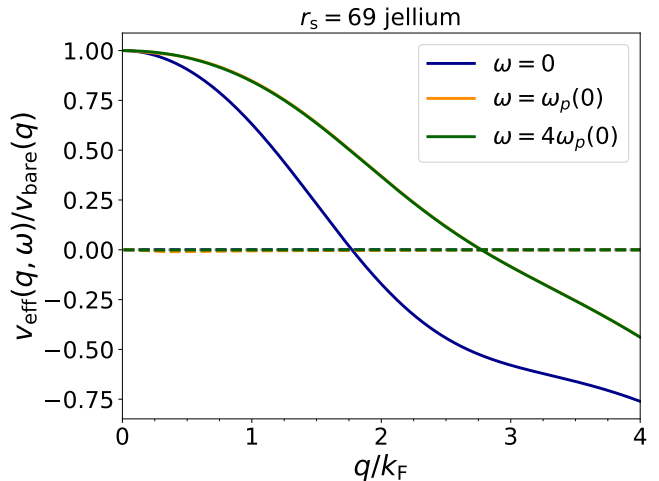


FIG. 8. Real (solid) and imaginary (dashed) parts of the scaled effective potential $v_{\text{eff}}/v_{\text{bare}}$ for $r_s = 69$ bulk jellium with the TC21 kernel. The crossings are $\text{Re } v_{\text{eff}}(1.773k_F, 0) = 0$, $\text{Re } v_{\text{eff}}(2.776k_F, \omega_p(0)) = 0$, and $\text{Re } v_{\text{eff}}(2.772k_F, 4\omega_p(0)) = 0$.

A collective mode corresponding to $\tilde{\epsilon}(q) < 0$, where $\tilde{\epsilon}(q)$ is the static dielectric function, has been called a “ghost plasmon” [42], and it was found that this mode competes with the plasmon mode at intermediate densities, $r_s \approx 22$ [43]. Given that the mode emerges from poles of $\tilde{\epsilon}(q, \omega)$ at conjugate imaginary frequencies [43], this excitation is better labeled as an exciton. (The name “ghost exciton” is eye-catching, but badly obscures *what* the collective mode represents. The original work [42] found that the collective mode contributes dominantly to the first-frequency-moment sum rule, and destabilizes the system.)

Further work [35] showed that the exciton appeared in the ALDA static response, but not in the RPA response. Their work demonstrated that inclusion of two-particle, two-hole ($2p2h$) excitations in a Fermi hypernetted chain-correlated basis function calculation of bulk jellium indeed produces an excitonic mode at intermediate densities. Figure 14 of Appendix C shows that the MCP07 and TC21 kernels also miss this excitonic mode, but that the dynamic LDA of Qian and Vignale (QV) [44], which satisfies a different static limit than the GKI dynamic LDA, captures the excitonic mode. The QV kernel is discussed in Appendix C.

Consider instead the change in density δn due to a weak external perturbation δv_{ext} . Linear response dictates that

$$\delta n(q, \omega) = \chi_0(\mathbf{q}, \omega)\delta v_s(q, \omega) = \frac{\chi_0(\mathbf{q}, \omega)}{\tilde{\epsilon}(q, \omega)}\delta v_{\text{ext}}, \quad (46)$$

where

$$\delta v_s(q, \omega) = \delta v_{\text{ext}}(q, \omega) + v_{\text{eff}}(q, \omega) \delta n(q, \omega) \quad (47)$$

is the change in the Kohn-Sham potential due to the perturbation. δv_s describes how the density screens δv_{ext} , and thus can be used to describe screening in real systems.

IV. CONCLUSIONS

We have motivated, presented, and analyzed an exchange correlation kernel for use in TD-DFT and linear response calculations based on known exact constraints. This form is tightly constrained to reproduce accurate jellium correlation energies at all densities, a feat at which many common exchange-correlation kernels fail. As jellium contains much of the essential physics of metals, we anticipate that the TC21 kernel will accurately describe properties of real metals.

Both MCP07 and TC21 approximate the kernel of the spin-unpolarized fluid phase of jellium. At densities typical of valence electrons in metals, for which this phase is the ground-state, both kernels accurately model f_{xc} . At much lower densities, for which this phase is only metastable, the MCP07 structure factor deviates appreciably from that of the paramagnetic fluid phase. TC21 is constructed as an improvement upon MCP07 at all densities, but especially at these lower densities.

ACKNOWLEDGMENTS

The work of ADK was supported by the Department of Energy, Basic Energy Sciences, under grant No. DE-SC0012575, and by Temple University. The work of NKN and AR was supported by the U.S. National Science Foundation (NSF) under Grant No. DMR-1553022. The work of JPP was supported by NSF Grant DMR-1939528, with a contribution from Chemical Theory, Modeling, and Computation, Division of Chemistry.

CONFLICT OF INTEREST

The authors declare that they have no financial and no non-financial conflicts of interest.

CODE AVAILABILITY

The code used to fit the revised MCP07 kernel is made freely available at <https://github.com/esoteric-ephemera/tc21>.

DATA AVAILABILITY

The data used to generate plots of the revised kernel are available in the “published_data” directory of the code repository (<https://github.com/esoteric-ephemera/tc21>).

-
- [1] W. Kohn and L. J. Sham, *Phys. Rev.* **140**, A1133 (1965).
 - [2] E. Runge and E. K. U. Gross, *Phys. Rev. Lett.* **52**, 997 (1984).
 - [3] E. K. U. Gross and W. Kohn, *Phys. Rev. Lett.* **55**, 2850 (1985), and erratum, *Phys. Rev. Lett.* **57**, 923 (1986).
 - [4] M. Petersilka, U. J. Gossmann, and E. K. U. Gross, *Phys. Rev. Lett.* **76**, 1212 (1996).
 - [5] J. Sun, A. Ruzsinszky, and J. P. Perdew, *Phys. Rev. Lett.* **115**, 036402 (2015).
 - [6] A. Ruzsinszky, N. K. Nepal, J. M. Pitarke, and J. P. Perdew, *Phys. Rev. B* **101**, 245135 (2020).
 - [7] N. Iwamoto and E. K. U. Gross, *Phys. Rev. B* **35**, 3003 (1987).
 - [8] L. A. Constantin and J. M. Pitarke, *Phys. Rev. B* **75**, 245127 (2007).
 - [9] M. Corradini, R. Del Sole, G. Onida, and M. Palumbo, *Phys. Rev. B* **57**, 14569 (1998).
 - [10] D. C. Langreth and J. P. Perdew, *Phys. Rev. B* **15**, 2884 (1977).
 - [11] K. S. Singwi, M. P. Tosi, R. H. Land, and A. Sjölander, *Phys. Rev.* **176**, 589 (1968).
 - [12] S. Kurth and J. P. Perdew, *Phys. Rev. B* **59**, 10461 (1999).
 - [13] J. P. Perdew, A. Ruzsinszky, J. Sun, N. K. Nepal, and A. D. Kaplan, *Proc. Natl. Acad. Sci. U.S.A.* **118**, 10.1073/pnas.2017850118 (2021), <https://www.pnas.org/content/118/4/e2017850118.full.pdf>.
 - [14] D. M. Ceperley and B. J. Alder, *Phys. Rev. Lett.* **45**, 566 (1980).
 - [15] G. F. Giuliani and G. Vignale, *Quantum Theory of the Electron Liquid* (Cambridge University Press, Cambridge, 2005).
 - [16] J. Enkovaara, C. Rostgaard, J. J. Mortensen, J. Chen, M. Dułak, L. Ferrighi, J. Gavnholt, C. Glinsvad, V. Haikola, H. A. Hansen, H. H. Kristoffersen, M. Kuisma, L. A. H. L. Lehtovaara, M. Ljungberg, O. Lopez-Acevedo, P. G. Moses, J. Ojanen, T. Olsen, V. Petzold, N. A. Romero, J. Stausholm-Møller, M. Strange, G. A. Tritsarlis, M. Vanin, M. Walter, B. Hammer, H. Häkkinen, G. K. H. Madsen, R. M. Nieminen, J. K. Nørskov, M. Puska, T. T. Rantala, J. Schiøtz, K. S. Thygesen, and K. W. Jacobsen, *Phys.: Condens. Matter* **22**, 253202 (2010).
 - [17] V. Olevano, L. Reining, and F. Sottile, (2021), see the DP code at <http://www.dp-code.org/>.
 - [18] M. Vanzini, A. Aouina, M. Panholzer, M. Gatti, and L. Reining, arXiv:1903.07930 [cond-mat.other] (2021), arXiv:1903.07930.
 - [19] (2020), we thank D. M. Ceperley for a private communication.
 - [20] P. Nozières and D. Pines, *Nuovo Cimento* **9**, 470 (1958).
 - [21] D. C. Langreth and J. P. Perdew, *Solid State Commun.* **17**, 1425 (1975).
 - [22] J. Lindhard, *Dan. Mat. Fys. Medd.* **28**, 1 (1954).

- [23] M. A. L. Marques and E. K. U. Gross, Time-dependent density functional theory, in *A Primer in Density Functional Theory* (Springer, 2003) pp. 162 – 164.
- [24] J. P. Perdew and Y. Wang, Phys. Rev. B **45**, 13244 (1992).
- [25] J. P. Perdew and A. Zunger, Phys. Rev. B **23**, 5048 (1981).
- [26] M. Lein, E. K. U. Gross, and J. P. Perdew, Phys. Rev. B **61**, 13431 (2000).
- [27] B. Dabrowski, Phys. Rev. B **34**, 4989 (1986).
- [28] G. Niklasson, Phys. Rev. B **10**, 3052 (1974).
- [29] P. Vashishta and K. S. Singwi, Phys. Rev. B **6**, 875 (1972).
- [30] K. N. Pathak and P. Vashishta, Phys. Rev. B **7**, 3649 (1973).
- [31] K. Utsumi and S. Ichimaru, Phys. Rev. B **22**, 5203 (1980).
- [32] C. F. Richardson and N. W. Ashcroft, Phys. Rev. B **50**, 8170 (1994).
- [33] C. A. Kukkonen and A. W. Overhauser, Phys. Rev. B **20**, 550 (1979).
- [34] P. Gori-Giorgi and J. P. Perdew, Phys. Rev. B **69**, 041103 (2004).
- [35] M. Panholzer, M. Gatti, and L. Reining, Phys. Rev. Lett. **120**, 166402 (2018).
- [36] K. Chen and K. Haule, Nature Comm. **10**, 3725 (2019).
- [37] P. Gori-Giorgi, F. Sacchetti, and G. B. Bachelet, Phys. Rev. B **61**, 7353 (2000), and erratum, *ibid.* **66**, 159901 (2002).
- [38] O. V. Dolgov, D. A. Kirzhnits, and E. G. Maksimov, Rev. Mod. Phys. **53**, 81 (1981).
- [39] W. Kohn and J. M. Luttinger, Phys. Rev. Lett. **15**, 524 (1965).
- [40] C. F. Richardson and N. W. Ashcroft, Phys. Rev. B **55**, 15130 (1997).
- [41] P. Monthoux, D. Pines, and G. G. Lonzarich, Nature, 1177– (2007).
- [42] K. Takayanagi and E. Lipparini, Phys. Rev. B **56**, 4872 (1997).
- [43] Y. Takada, Phys. Rev. B **94**, 245106 (2016).
- [44] Z. Qian and G. Vignale, Phys. Rev. B **65**, 235121 (2002), erratum Phys. Rev. B **71**, 169904 (2005).
- [45] G. Ortiz and P. Ballone, Phys. Rev. B **50**, 1391 (1994).
- [46] S. Conti and G. Vignale, Phys. Rev. B **60**, 7966 (1999).
- [47] C. A. Ullrich and K. Burke, The Journal of Chemical Physics **121**, 28 (2004).
- [48] G. Vignale and W. Kohn, Phys. Rev. Lett. **77**, 2037 (1996).
- [49] R. Nifosi, S. Conti, and M. P. Tosi, Phys. Rev. B **58**, 12758 (1998).
- [50] N. K. Nepal, A. D. Kaplan, J. M. Pitarke, and A. Ruzsinszky, arXiv:2105.11451 [cond-mat.mtrl-sci] (2021), arXiv:2105.11451.
- [51] V. U. Nazarov, G. Vignale, and Y.-C. Chang, Phys. Rev. Lett. **102**, 113001 (2009).
- [52] P. W. Anderson, Science **177**, 393 (1972).

APPENDIX A: PLOTS OF THE TC21 DIELECTRIC FUNCTION AND RELATED QUANTITIES

The plasmon dispersion curves, plotted in Fig. 9, were made by zeroing out the dielectric function at complex frequencies $\omega = u + iv$ (with u, v both real)

$$\tilde{\epsilon}(q, u + iv) \approx 1 - \left[\frac{4\pi}{q^2} + f_{xc}(q, u) - v \frac{\partial \text{Im} f_{xc}(q, u)}{\partial u} + iv \frac{\partial \text{Re} f_{xc}(q, u)}{\partial u} \right] \chi_0(q, u + iv), \quad (48)$$

where a low-order Taylor expansion of $f_{xc}(q, u)$ has been made to analytically continue the kernel to complex frequencies just below the real axis. Without simplification, the Taylor series of $f_{xc}(q, u)$ would be

$$f_{xc}(q, u + iv) \approx f_{xc}(q, u_0) + (u + iv - u_0) \frac{df_{xc}}{du_0}(q, u_0) \quad (49)$$

with u_0 a real frequency. In this calculation, we use the Taylor expansion from $u_0 = u$ to analytically continue the kernel only to imaginary frequencies. This is more rigorous than the procedure used in Ref. [6], which used a Taylor series about u_0 , and varied u and v . That procedure assumes the low-order Taylor series about u_0 also has validity for $u \neq u_0$, which cannot be the case generally.

With that simplification

$$f_{xc}(q, u + iv) \approx f_{xc}(q, u) + iv \frac{\partial f_{xc}}{\partial u}(q, u) \quad (50)$$

$$f_{xc}(q, u + iv) \approx f_{xc}(q, u) + iv \left[\frac{\partial \text{Re} f_{xc}}{\partial u}(q, u) + i \frac{\partial \text{Im} f_{xc}}{\partial u}(q, u) \right]. \quad (51)$$

As the plasmon frequencies lie just below the real axis, a two-dimensional Newton-Raphson method was used to zero out both components of the dielectric function simultaneously. The Jacobian matrix

$$\mathbf{J} = \begin{pmatrix} \frac{\partial \text{Re} \tilde{\epsilon}}{\partial u} & \frac{\partial \text{Re} \tilde{\epsilon}}{\partial v} \\ \frac{\partial \text{Im} \tilde{\epsilon}}{\partial u} & \frac{\partial \text{Im} \tilde{\epsilon}}{\partial v} \end{pmatrix} \quad (52)$$

was calculated numerically. Then, given a guess of the plasmon frequency $\omega_{p,j}(q) = u_j + iv_j$, the next guess for the plasmon frequency would be

$$\begin{pmatrix} u_{j+1} \\ v_{j+1} \end{pmatrix} = (\mathbf{1} - \mathbf{J}^{-1}) \begin{pmatrix} u_j \\ v_j \end{pmatrix}. \quad (53)$$

The root finding algorithm stopped either when no roots could be found, or when [6]

$$\text{Re } \omega_p(q) = \frac{1}{2}q^2 + k_F q, \quad (54)$$

indicating that the energies of the plasmon and a particle-hole pair were degenerate. In all cases, we have found that the numerical procedure failed before the particle-hole continuum condition was met.

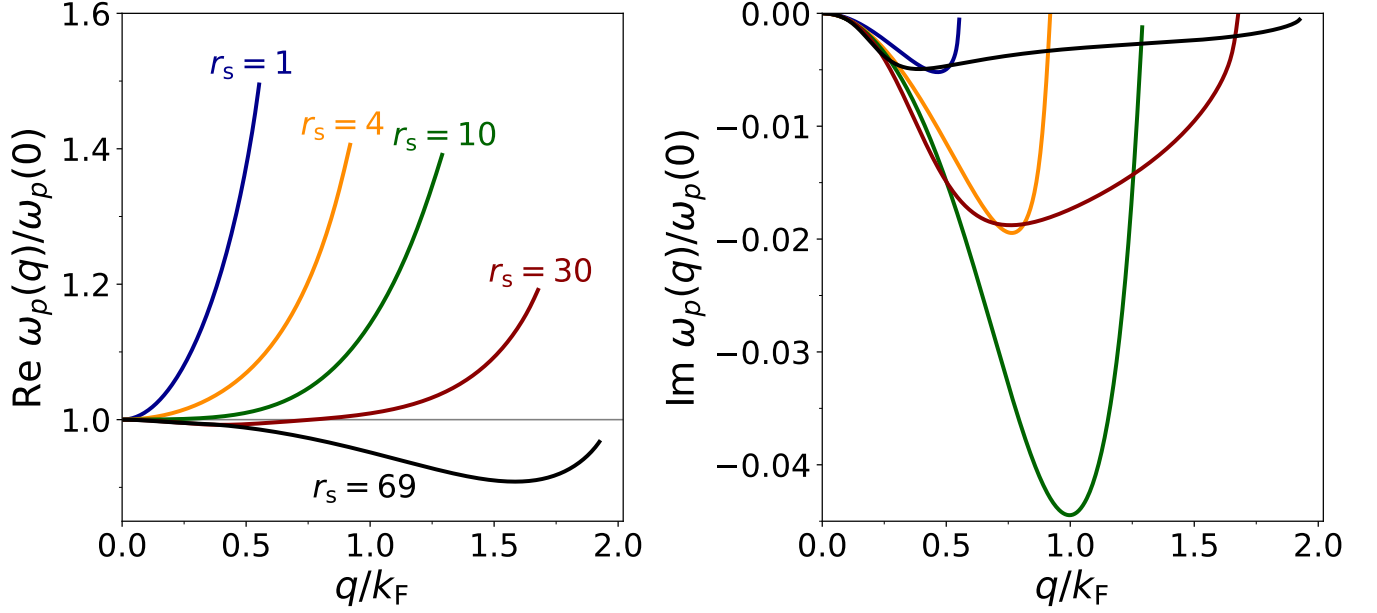


FIG. 9. Real (left) and imaginary (right) parts of the TC21 plasmon dispersion frequency $\text{Re } \omega_p(q)$ such that $|\tilde{\epsilon}^{\text{TC21}}(q, \omega)| < 10^{-6}$, with $\tilde{\epsilon}$ given by Eq. 45.

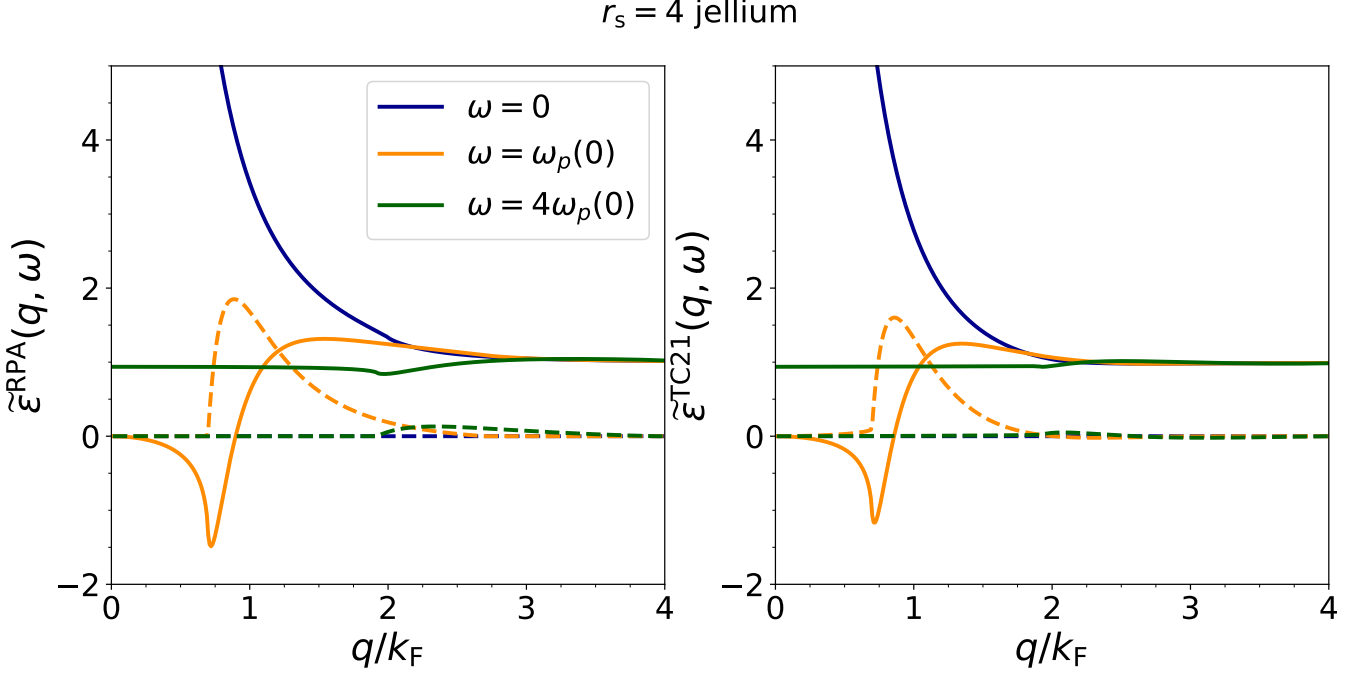


FIG. 10. Real (solid) and imaginary (dashed) parts of the RPA (left) and TC21 (right) dielectric functions $\tilde{\epsilon}(q, \omega) = 1 - [\frac{4\pi}{q^2} + f_{xc}(q, \omega)]\chi_0(q, \omega)$ for $\omega = 0$, $\omega_p(0)$, and $4\omega_p(0)$, for $r_s = 4$ jellium.

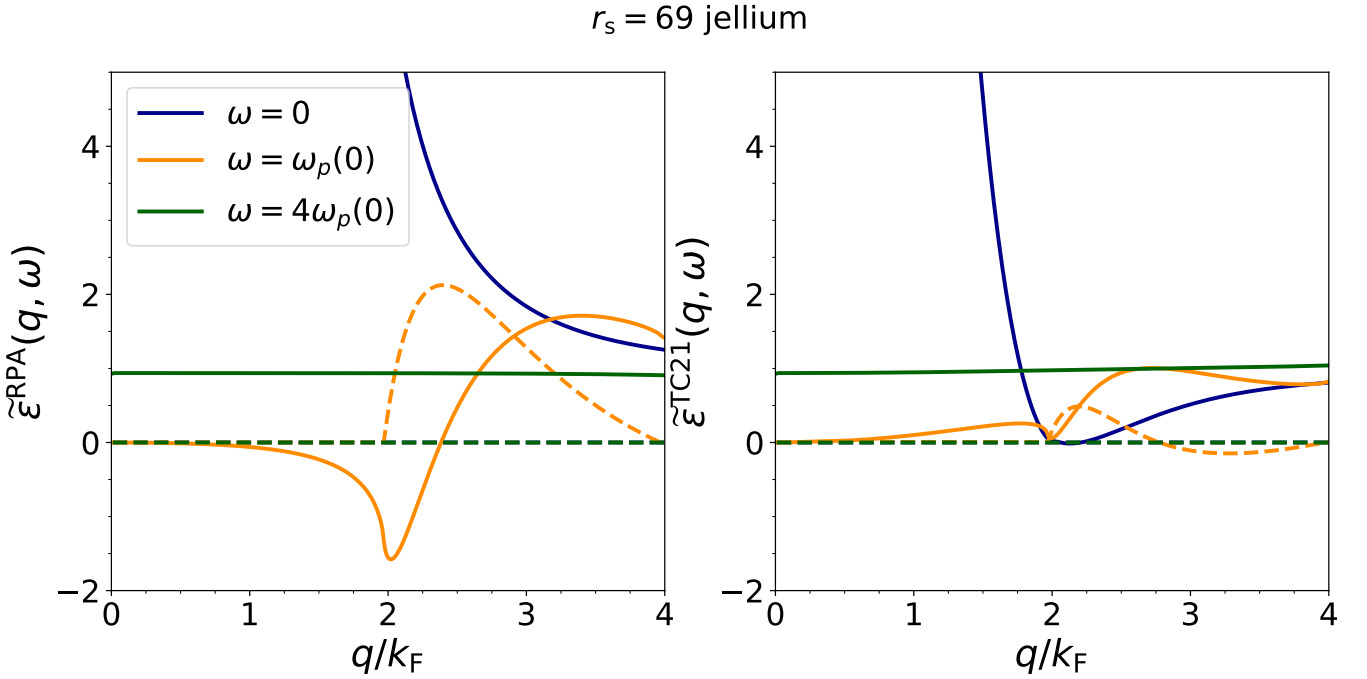


FIG. 11. Real (solid) and imaginary (dashed) parts of the RPA (left) and TC21 (right) dielectric functions $\tilde{\epsilon}(q, \omega) = 1 - [\frac{4\pi}{q^2} + f_{xc}(q, \omega)]\chi_0(q, \omega)$ for $\omega = 0$, $\omega_p(0)$, and $4\omega_p(0)$, for $r_s = 69$ jellium.

Appendix A: The jellium spectral function from QMC data

This section presents previously unpublished QMC data of the spectral function, or static structure factor $S(q)$ of jellium, at lower densities, $r_s \gg 10$. A detailed discussion of the QMC computational methods used is given in Ref. [45]. These results are plotted in Fig. 12, and show that the peak structure in $S(q)$ at intermediate-to low-density jellium is not as pronounced as in the MCP07 spectral function.

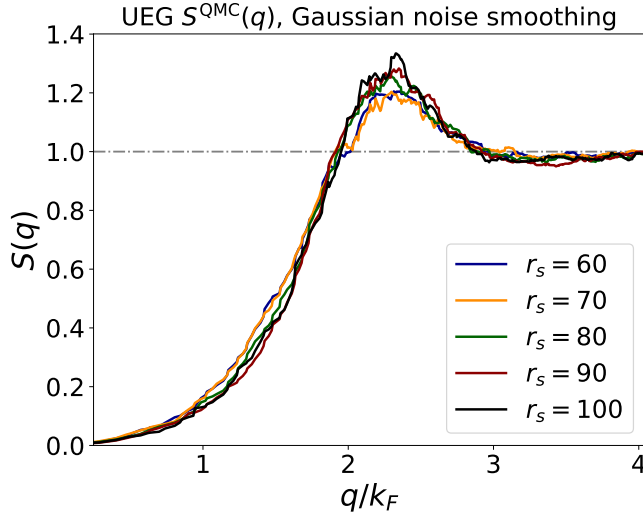


FIG. 12. Previously unpublished QMC data of the static structure factor $S(q)$ in jellium [19] at lower densities. The data has been smoothed by assuming a Gaussian noise distribution around each point. See the discussion around Eq. A1. These results are for the spin-polarized fluid phase, which was found to be more stable than the spin-unpolarized fluid phase for $75 \leq r_s \leq 100$ in Ref. [14], and for $60 \leq r_s \leq 100$ in Ref. [45].

Note that the data in Fig. 12 has been smoothed in the following manner, which we call Gaussian noise smoothing. Suppose we sample $S(q)$ at M points q_0, q_1, \dots, q_M , and consider the value of $S(q_i)$ to be correlated to its $2N$ -nearest neighbors, at most (by virtue of smoothness). Let $N_L \equiv \max(0, i - N)$ and $N_U \equiv \min(M, i + N)$. Then the smoothed $\tilde{S}(q_i)$ is given by

$$\tilde{S}(q_i) = W^{-1} \sum_{j=N_L}^{N_U} S(q_j) \exp \left\{ \frac{[S(q_j) - \mu_i]^2}{\sigma_i} \right\} \quad (\text{A1})$$

$$W = \sum_{j=N_L}^{N_U} \exp \left\{ \frac{[S(q_j) - \mu_i]^2}{\sigma_i} \right\} \quad (\text{A2})$$

for $i = 0, 1, \dots, M$, where

$$\mu_i = \frac{1}{N_U - N_L + 1} \sum_{j=N_L}^{N_U} S(q_j) \quad (\text{A3})$$

$$\sigma_i = \frac{1}{N_U - N_L + 1} \sum_{j=N_L}^{N_U} S(q_j)^2 - \mu_i^2. \quad (\text{A4})$$

For $q/k_F < 1$, $N = 1$, and for $q/k_F \geq 1$, $N = 4$. These values were chosen to make a reasonable compromise between data fidelity and readability. The limit $S(q \rightarrow 0) \rightarrow 0$ is lost when N is increased beyond 1 in this range. Conversely, the raw data (available on the code repository) was too oscillatory near the peak in each curve to be easily interpreted, and thus a larger value of N was needed to smooth the larger, likely unrealistic oscillations. However, increasing N beyond 4 was found to break the limit $S(q \rightarrow \infty) \rightarrow 1$.

This method of data smoothing is similar to data binning, but with a generalized weight function. Data binning would replace Eq. A1 with a simple average,

$$\tilde{S}_{\text{bin}}(q_i) = \frac{1}{N_U - N_L} \sum_{j=N_L}^{N_U} S(q_j), \quad (\text{A5})$$

a method we also tried. However, a simple binning method resulted in lower data fidelity (i.e., too much loss).

Appendix B: The order of limits issue

The static $\omega \rightarrow 0$, long-wavelength $q \rightarrow 0$ limit of $f_{\text{xc}}(q, \omega)$ appears to be non-unique. As was derived by Gross and Kohn, [3]

$$\lim_{\omega \rightarrow 0} \lim_{q \rightarrow 0} f_{\text{xc}}(q, \omega) = \frac{d^2}{dn^2} [n \varepsilon_{\text{xc}}^{\text{LDA}}(n)] \equiv f_{\text{xc}}^{\text{ALDA}}(r_s), \quad (\text{B1})$$

from the compressibility sum rule, where $\varepsilon_{\text{xc}}^{\text{LDA}}(n)$ is the LDA exchange-correlation energy per electron in jellium. However, as was shown by Conti and Vignale [46], in the reverse limit

$$\lim_{\omega \rightarrow 0} \lim_{q \rightarrow 0} f_{\text{xc}}(q, \omega) = f_{\text{xc}}^{\text{ALDA}}(r_s) + \frac{\mu_{\text{xc}}(r_s)}{n^2}, \quad (\text{B2})$$

where $\mu_{\text{xc}}(r_s)$ is the XC shear modulus of bulk jellium. Clearly, both limits agree when $\mu_{\text{xc}}(r_s) = 0$, however it is unclear what the physical consequences of this assumption would be; the excitation energies of atoms are not described optimally by $f_{\text{xc}}^{\text{ALDA}}$, nor a longitudinal $f_{\text{xc}}(\omega)$ with $\mu_{\text{xc}} = 0$, nor with $|\mu_{\text{xc}}(r_s)| > 0$ [47].

Within time-dependent current density functional theory [48], there exist two kernels in the linear response regime: a longitudinal kernel f_{xc}^{L} that is identified with the scalar f_{xc} of TD-DFT, and a transverse XC kernel f_{xc}^{T} . In this framework, [46]

$$\lim_{\omega \rightarrow 0} \lim_{q \rightarrow 0} f_{\text{xc}}^{\text{T}}(q, \omega) = \frac{\mu_{\text{xc}}(r_s)}{n^2}, \quad (\text{B3})$$

thus even when $\mu_{xc}(r_s)$ is set to zero, an approximation for $f_{xc}^T(q, \omega)$ can estimate the value of $\mu_{xc}(r_s)$. At present, reliable estimates exist only in a limited range of metallic densities [44, 49], however $\mu_{xc}(r_s)/n^2 \ll |f_{xc}^{ALDA}(r_s)|$.

We wish to compare the dynamic GKI kernel with the (longitudinal) dynamic kernel of Qian and Vignale (QV) [44]. The GKI kernel recovers the order of limits $q \rightarrow 0$ then $\omega \rightarrow 0$, whereas the QV kernel recovers the opposite order of limits. Moreover, the QV kernel promises a more correct treatment of two-plasmon excitations [44] by using a GKI-like frequency interpolation plus a Gaussian correction,

$$\text{Im } f_{xc}(\omega) = -\frac{2\omega_p(0)}{n} \left\{ \frac{a(r_s)\tilde{\omega}}{[1 + b(r_s)\tilde{\omega}^2]^{5/4}} + \tilde{\omega}^3 \exp \left[-\frac{(|\tilde{\omega}| - \Omega(r_s))^2}{\Gamma(r_s)} \right] \right\} \quad (\text{B4})$$

where $\tilde{\omega} = \omega/[2\omega_p(0)]$ and $\omega_p(0) = \sqrt{4\pi n}$ is the semi-classical plasmon frequency. The parameters $a(r_s)$, $b(r_s)$, $\Gamma(r_s)$, and $\Omega(r_s)$ are constrained by a set of equations. There are solutions for $a(r_s)$ and $b(r_s)$ for all r_s , however there are no solutions for $\Gamma(r_s)$ and $\Omega(r_s) = 1 - 3\Gamma(r_s)/2$ above a critical $r_{s,c}$.

Just like the GKI kernel, the QV kernel requires ALDA input; it also requires input for $\mu_{xc}(r_s)$ at arbitrary r_s . Equation 11 of Ref. [50] parametrized $\mu_{xc}(r_s)$

$$\frac{\mu_{xc}(r_s)}{n} = \frac{a}{r_s} + (b - a) \frac{r_s}{r_s^2 + c}, \quad (\text{B5})$$

with $a = 0.031152$, $b = 0.011985$, and $c = 2.267455$; we will use their parametrization here. (Ref. [46] presented a similar fit in Eq. 4.9 of their work, but their parameters appear to be in significant error.) The value of $r_{s,c}$ above which no solutions exist for $\Gamma(r_s)$ and $\Omega(r_s)$ will depend on the particular f_{xc}^{ALDA} and $\mu_{xc}(r_s)$ used; if $\mu_{xc}(r_s) = 0$ for all r_s , then $r_{s,c} \approx 45.2$, whereas if Eq. B5 is used, $r_{s,c} \approx 56.2$.

For all $r_s > r_{s,c}$, we are forced to set $\Gamma = \epsilon$, where ideally $\epsilon = 0$, but in practice $\epsilon = 10^{-14}$. This yields essentially a double-delta function resonance at $\omega = \pm 2\omega_p(0)$, signaling onset of a two-plasmon excitation. As seen in Fig. 13, the value of $\Gamma(r_s)$ abruptly falls to zero for $r_s > r_{s,c}$.

The QV kernel is able to capture excitonic excitations, due to the Gaussian term in Eq. B4, which reduces to a delta-function resonance at low densities. Figure 14 shows that the QV kernel predicts the emergence of a ‘‘ghost exciton’’ in intermediate density jellium.

For reasons that have been described in the Introduction, we have not fitted a QV-MCP07 kernel, where the frequency-dependence of the GKI kernel is replaced by that of the QV kernel. Whereas we can easily deduce a parameterization of the real part of the GKI kernel that is independent of r_s , and thus also a reasonable parameterization of its continuation to imaginary frequencies,

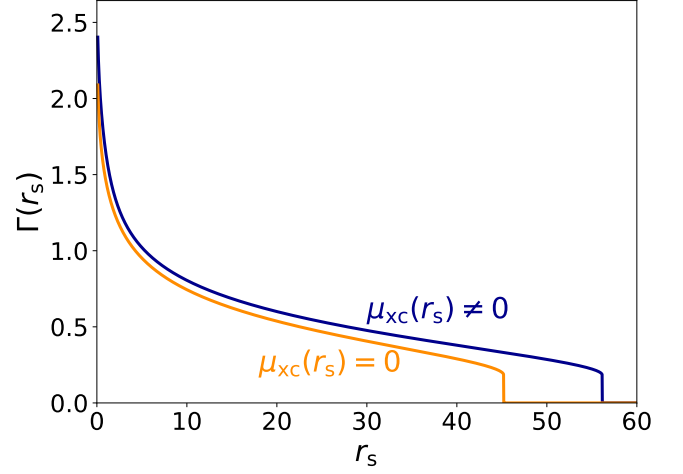


FIG. 13. The $\Gamma(r_s)$ parameter in the dynamic, long-wavelength Qian and Vignale [44] kernel. Above a critical r_s , no solutions for $\Gamma(r_s)$ can be found consistent with the constraints placed on the kernel. Above this value, we have set $\Gamma = 0$; the transition is abrupt, and dependent upon the ALDA used, as well as the XC shear modulus.

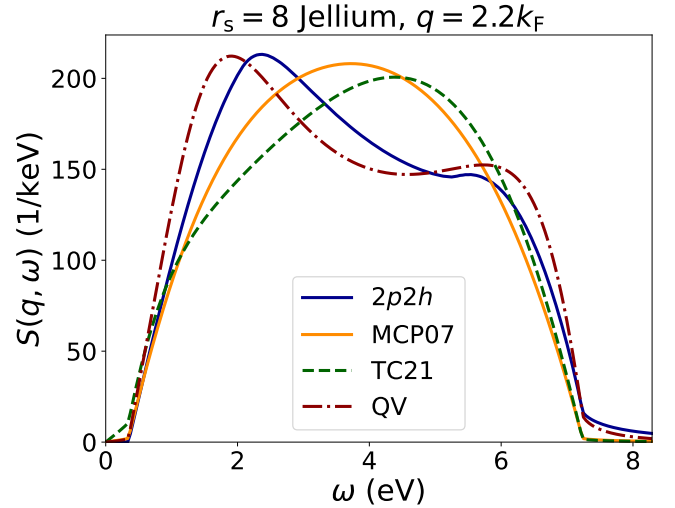


FIG. 14. Comparison of the dynamic structure factor $S(q = 2.2k_F, \omega)$ for various model kernels for $r_s = 8$ jellium, analogous to Fig. 2 of Ref. [35]. The ghost exciton can be observed as a double-peak structure in the $2p2h$ data and QV kernel only.

a similar procedure cannot be done for the QV kernel. The GKI-like part of the QV kernel can be expressed using Eq. 15, however the real part of the Gaussian term cannot be expressed in an r_s -independent form, nor can the real part be computed analytically. We found that a low-order Taylor expansion of the real part of the kernel rapidly breaks down for $\omega/\omega_p(0) \ll 1$, and is thus not useful in a Padé-like approximant.

The TC21 fitting involves only a three-dimensional integration that can be rapidly expedited using modern

single instruction, multiple data (SIMD) parallel computation. The QV-MCP07 fitting would involve a five-dimensional numeric integration at each value of the interaction-strength-scaled frequency, which cannot be easily parallelized via SIMD.

Appendix C: Ultralocality coefficient

As in Ref. [50], this section computes the ultralocality coefficient $\alpha(\omega)$ [51]

$$\lim_{|q| \rightarrow 0} f_{xc}(q, \omega) = -\frac{4\pi\alpha(\omega)}{q^2}. \quad (\text{C1})$$

$\alpha(\omega)$ is the frequency-dependent strength of the long-range part of f_{xc} . It vanishes for a uniform density. For a weakly-inhomogeneous density, such as that of a real simple metal, we have computed $\alpha(\omega)$ by the formula of Ref. [51]. For an insulator, $\alpha(\omega)$ has major effect on optical absorption.

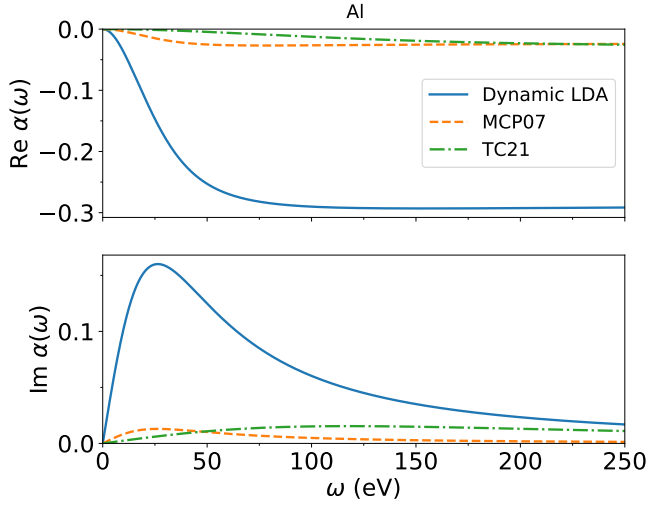


FIG. 15. The ultralocality coefficient $\alpha(\omega)$ in face-centered cubic Al, using the same pseudopotential density as was used in Ref. [50]. The dynamic LDA refers to the GKI frequency-dependent kernel, but using Eq. 15 to model the real part of $f_{xc}(q=0, \omega)$, and with PW92 for the ALDA.

Appendix D: Density fluctuations

As we have emphasized here, the static structure factor $S(q)$ is of great importance for understanding emergent phenomena in solids. That analysis neglects the role of the dynamic structure factor $S(q, \omega)$. Reference [13] suggested that the following frequency moments, weighted

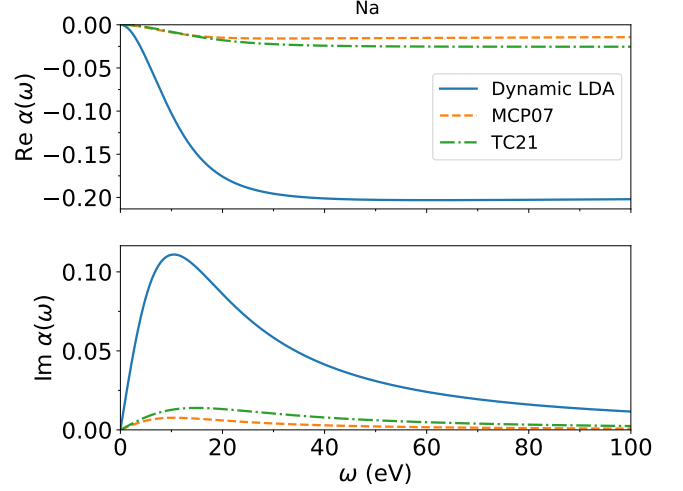


FIG. 16. The ultralocality coefficient $\alpha(\omega)$ in body-centered cubic Na, using the same pseudopotential density as was used in Ref. [50].

by $S(q)$,

$$\langle \omega_p(q) \rangle = \left[\int_0^\infty S(q, \omega) d\omega \right]^{-1} \int_0^\infty S(q, \omega) \omega d\omega \quad (\text{D1})$$

$$\langle \omega_p(q) \rangle = S(q)^{-1} \int_0^\infty S(q, \omega) \omega d\omega \quad (\text{D2})$$

$$\langle \Delta \omega_p(q) \rangle = \left[S(q)^{-1} \int_0^\infty S(q, \omega) \omega^2 d\omega - \langle \omega_p(q) \rangle^2 \right]^{1/2} \quad (\text{D3})$$

could describe the average and standard deviation in the frequency of a density fluctuation, respectively. Their analysis demonstrated that, in low density jellium, the average frequency of a density fluctuation abruptly drops towards zero for $q \approx 2k_F$. This would suggest the emergence of a crystalline phase at low density within Anderson's [52] interpretation of symmetry breaking: Fluctuations in the density of a large number of electrons can abruptly freeze, signaling the onset of an observable symmetry broken phase that would not be observable in a system of few electrons.

This behavior can be observed in Fig. 17 for the MCP07 kernel. Interestingly, the TC21 value of $\langle \omega_p(q) \rangle$ does not drop to zero at $r_s = 69$. Figure 18 displays $\langle \Delta \omega_p(q) \rangle$.

Therefore the TC21 kernel does not describe the low-density fluctuations of jellium well, at least within Anderson's theory. This is due to the scaling function $p(q, r_s)$ of Eq. 31. $p(q, r_s)$ decreases the rate at which $f_{xc}(0, \Omega)$ approaches its infinite frequency limit for $r_s < 1/C^{1/2} \approx 4.732$ bohr. Conversely, for $r_s > 1/C^{1/2}$, $f_{xc}(0, \Omega)$ more rapidly approaches its infinite frequency limit. This behavior, while seemingly necessary for the recovery of accurate correlation energies, introduces roots into the effective dielectric function $\tilde{\epsilon}$, as seen in Fig. 11.

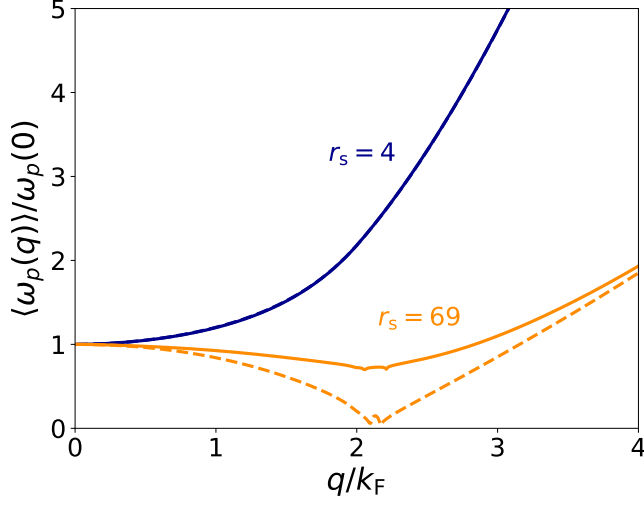


FIG. 17. Average density fluctuation $\langle \omega_p(q) \rangle$ in bulk jellium for the MCP07 (dashed) and TC21 (solid) kernels. The curves essentially coincide at $r_s = 4$, but differ sharply at $r_s = 69$.

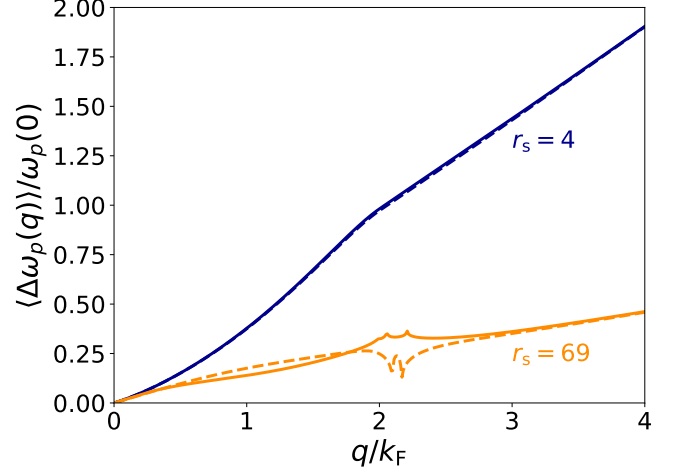


FIG. 18. Standard deviation in the density fluctuation $\langle \Delta \omega_p(q) \rangle$ in bulk jellium for the MCP07 (dashed) and TC21 (solid) kernels. The curves mostly coincide at $r_s = 4$ and differ in slope and concavity at $r_s = 69$.

This behavior can also be tied to the spectral function $S(q)$ at lower densities. Consider Fig. 12, which plots $S^{\text{QMC}}(q)$ for the spin-polarized fluid phase. Although $S^{\text{TC21}}(q)$, plotted in Fig. 3, and $S^{\text{MCP07}}(q)$, plotted in Fig. 2, are for the spin-unpolarized fluid phase, it is clear that TC21 gives a more realistic description of the ground state $S(q)$ than does MCP07. This is because the peak structure in $S^{\text{MCP07}}(q)$ is softened dramatically in $S^{\text{TC21}}(q)$. This softening is also observed in Fig. 17, where the average frequency of a plasmon is much smoother in TC21, never dropping to zero frequency.